Conformational Spread as a Mechanism for Cooperativity in the Bacterial Flagellar Switch

Fan Bai, *et al.*

Science **327**, 685 (2010);
DOI: 10.1126/science.1182105

study, but our results imply that many insects may be capable of moving between winter- and summer-breeding sites (~2000 km) in just three or four successive 8-hour migratory flights. These insect migrants are clearly very successful: We estimate that at least 2.3 billion individuals were involved in the high-altitude mass migrations recorded between 2000 and 2007, with ~1.5 times as many individuals involved in fall return migrations as in spring influxes (SOM text). Considering that many migrant insects are important agricultural pests and that the frequency of insect migration to northern latitudes, associated with climate change, is increasing (*19*, *23*), our ability to understand and predict migration strategies will become progressively more important.

References and Notes

1. T. Alerstam, *Science* **313**, 791 (2006).
2. S. Åkesson, A. Hedenström, *Bioscience* **57**, 123 (2007).
3. K. Aarestrup *et al.*, *Science* **325**, 1660 (2009).
4. R. A. Holland, M. Wikelski, D. S. Wilcove, *Science* **313**, 794 (2006).
5. C. R. Wood *et al.*, *Int. J. Biometeorol.* **50**, 193 (2006).
6. J. W. Chapman *et al.*, *Curr. Biol.* **18**, 514 (2008).
7. J. W. Chapman *et al.*, *Curr. Biol.* **18**, R908 (2008).
8. R. T. Cardé, *Curr. Biol.* **18**, R472 (2008).
9. R. B. Srygley, R. Dudley, *Integr. Comp. Biol.* **48**, 119 (2008).
10. K. Mikkola, *Entomol. Fenn.* **14**, 15 (2003).
11. C. Stefanescu, M. Alarcón, A. Àvila, *J. Anim. Ecol.* **76**, 888 (2007).
12. H. Mouritsen, B. J. Frost, *Proc. Natl. Acad. Sci. U.S.A.* **99**, 10162 (2002).
13. C. Merlin, R. J. Gegear, S. M. Reppert, *Science* **325**, 1700 (2009).
14. R. L. Nesbit *et al.*, *Anim. Behav.* **78**, 1119 (2009).
15. J. W. Chapman, D. R. Reynolds, A. D. Smith, *Int. J. Pest Manage.* **50**, 225 (2004).
16. Materials and methods are available as supporting material on *Science* Online.
17. J. W. Chapman, D. R. Reynolds, A. D. Smith, E. T. Smith, I. P. Woiwod, *Bull. Entomol. Res.* **94**, 123 (2004).
18. C. R. Wood *et al.*, *Bull. Entomol. Res.* **99**, 525 (2009).
19. E. Pollard, J. N. Greatorex-Davies, *Ecol. Lett.* **1**, 77 (1998).
20. M. Green, T. Alerstam, *J. Theor. Biol.* **218**, 485 (2002).
21. M. Green, *Ardea* **92**, 145 (2004).
22. H. Schmaljohann, F. Liechti, B. Bruderer, *Behav. Ecol. Sociobiol.* **63**, 1609 (2009).
23. T. H. Sparks, D. B. Roy, R. L. H. Dennis, *Glob. Change Biol.* **11**, 507 (2005).

24. We thank S. Clark, L. Castle, D. Ladd, P. Clark, G. Hays, J. Phillips, T. Alerstam, D. Thomson, and M. Hort. Rothamsted Research receives grant-aided support from U.K. Biotechnology and Biological Sciences Research Council.

Supporting Online Material

www.sciencemag.org/cgi/content/full/327/5966/682/DC1
Materials and Methods
SOM Text
Figs. S1 to S8
Tables S1 to S5
References

7 October 2009; accepted 14 December 2009
10.1126/science.1182990

Conformational Spread as a Mechanism for Cooperativity in the Bacterial Flagellar Switch

Fan Bai,[1,2]* Richard W. Branch,[1]* Dan V. Nicolau Jr.,[3,4]* Teuta Pilizota,[1,5] Bradley C. Steel,[1] Philip K. Maini,[3,6] Richard M. Berry†[1]

The bacterial flagellar switch that controls the direction of flagellar rotation during chemotaxis has a highly cooperative response. This has previously been understood in terms of the classic two-state, concerted model of allosteric regulation. Here, we used high-resolution optical microscopy to observe switching of single motors and uncover the stochastic multistate nature of the switch. Our observations are in detailed quantitative agreement with a recent general model of allosteric cooperativity that exhibits conformational spread—the stochastic growth and shrinkage of domains of adjacent subunits sharing a particular conformational state. We expect that conformational spread will be important in explaining cooperativity in other large signaling complexes.

The elements of protein signaling networks are often complexes that change their activity in response to binding specific ligands. Multisubunit protein complexes often show cooperativity, with either binding or activity showing a switchlike sigmoidal dependence upon ligand concentration. Cooperativity has classically been understood in terms of the concerted (*1*) or sequential (*2*) models of allosteric regulation, which describe coupling between ligand binding and subunit conformation, and coupling of conformations between different subunits. Both models have deterministic elements. In the concerted model, coupling between subunits is absolute: All subunits switch conformation simultaneously. In the sequential model, coupling between ligand binding and conformation is absolute: When a ligand binds a subunit, that subunit switches. More recently, a mathematical model of the general allosteric scheme proposed by Eigen (*3*) was constructed in which both types of coupling are probabilistic (*4*, *5*). This model encompasses the classical mechanisms at its limits and introduces the mechanism of conformational spread, with domains of a particular conformational state growing or shrinking faster than ligand binding. Although the classical models have been useful in explaining the regulation of numerous oligomeric proteins (*6*, *7*), conformational spread is a natural extension that will be necessary for understanding cooperativity in large multimeric protein complexes (*4*, *8*).

The bacterial switch complex in *Escherichia coli* is a large protein ring that controls the direction of rotation of the bacterial flagellar motor (*9*) (Fig. 1A). The switch response shows a steep sigmoidal relationship between the concentration of the response regulator CheY-P and motor rotational bias (the fraction of time spent rotating in a given direction), contributing to the remarkable gain of the bacterial chemotactic network (*10*, *11*). Binding of CheY-P to FliM protein subunits of the complex is much less cooperative [Hill coefficient <2 (*12*, *13*)] than the switch response [Hill coefficient 10.1 (*10*)]. In terms of classical allosteric regulation theory, this precludes the sequential model and favors the concerted model, where the binding cooperativity can be less than the response cooperativity (*14*). Further evidence against the sequential model is that flagellar motors can switch at low temperatures in the absence of CheY (*15*).

Consistent with the concerted model, the flagellar switch has traditionally been understood in binary terms, with instantaneous switching between stable counterclockwise (CCW) and clockwise (CW) rotation (*16*–*20*). However, it is difficult to imagine a mechanism for instantaneous concerted transitions of such a large complex without invoking action at a distance. A conformational spread model of the flagellar switch has been constructed (*4*) that, in contrast to the two-state concerted model, allows for a multistate switch (Fig. 1, B to D). The directly observable consequence of conformational spread in this system is that switch events should be non-instantaneous with broadly distributed durations due to the biased random walk of conformational spread. Additionally, incomplete switches due to rapid incomplete growth and shrinkage of nucleated domains should be observable as transient speed fluctuations in otherwise stable rotation.

[1]Clarendon Laboratory, Department of Physics, University of Oxford, Parks Road, Oxford OX1 3PU, UK. [2]Nanobiology Laboratories, Graduate School of Frontier Biosciences, Osaka University, 1-3 Yamadaoka, Suita, Osaka, 565-0871 Japan. [3]Centre for Mathematical Biology, Mathematical Institute, University of Oxford, St. Giles, Oxford OX1 3LB, UK. [4]Department of Integrative Biology, Valley Life Sciences Building, University of California–Berkeley, Berkeley, CA 94708, USA. [5]Carl Icahn Laboratory, Princeton University, Washington Road, Princeton, NJ 08644, USA. [6]Oxford Centre for Integrative Systems Biology, Department of Biochemistry, South Parks Road, Oxford OX1 3QU, UK.

*These authors contributed equally to this work.
†To whom correspondence should be addressed. E-mail: r.berry1@physics.ox.ac.uk

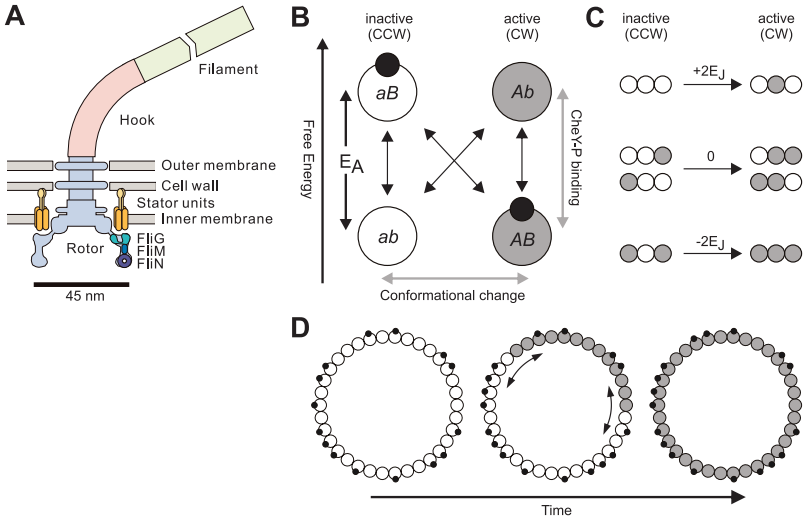

Fig. 1. Structure and conformational spread model of the bacterial flagellar switch. (**A**) Schematic of the *E. coli* bacterial flagellar motor. Indicated are the likely positions of switch complex proteins FliG (~26 copies), FliM (~34 copies), and FliN (~136 copies) and the torque-generating stator units $MotA_4MotB_2$ (~10 copies, orange) (*9*). Structural studies indicate that conformational changes in FliM upon binding of the signaling molecule CheY-P are coupled indirectly to conformational changes in the FliG track, which interfaces with the torque-generating units to determine rotation direction (*21*, *34*–*36*). We consider the switch complex to be a ring of 34 identical protomers, each consisting of ~1 FliG, 1 FliM, and a tetramer of FliN subunits. Each protomer possesses a single binding site to which a CheY-P molecule can be bound (*B*) or not bound (*b*) and has two conformations, active (*A*, corresponding to CW rotation) or inactive (*a*, CCW). (**B**) A free-energy diagram of the four states of a protomer and the transitions between them, for the case of CW bias = 0.5. For simplicity, we consider the symmetrical case where the magnitude of the free-energy difference between favored and unfavored states (E_A) is the same with or without CheY-P (black circle) bound. (**C**) Interactions between adjacent protomers favor pairs with the same conformation. We assume that the free energy of interaction is lower by E_J for any like pair compared to any unlike pair, independent of CheY-P binding. These interactions add 0, $+2E_J$ or $-2E_J$ to the free energy of a conformational change, depending on the state of adjacent protomers. (**D**) Above a critical value of E_J the ring spends the majority of time in a coherent state, occasionally stochastically switching between CCW and CW configurations. Switches typically occur by a single nucleation of a new domain, followed by conformational spread of the domain, which follows a biased random walk until it either encompasses the entire ring or collapses back to the previous coherent state (Movie S1). The model behaves like the classical sequential model in the limit of large E_A (absolute coupling between binding and conformation) and like the classical concerted model in the limit of large E_J (absolute coupling between subunit conformations).

Recent technical advances have allowed us to observe these signatures of conformational spread. We investigated motor switching using back-focal-plane interferometry of polystyrene beads attached to truncated flagella of *E. coli* (*21*–*23*), with ~1° angular resolution and ~1 ms time resolution, limited by the mechanical relaxation of beads attached by the elastic flagellar hook (*22*). Single motors with a steady bead trajectory were recorded for 30 s to minimize photo damage and sensitivity to slow fluctuations in bias (*24*), and then were categorized by bias (*20*, *22*). Angles and radii of the bead trajectory were obtained by fitting an ellipse to the trajectory, and then converted to instantaneous motor speed (*22*).

Median filtered motor speed records show complete switching between CW and CCW states and incomplete switching to speed levels in between (Fig. 2A, left panel). The multistate nature of the record renders traditional zero-crossing analyses of motor switching (*18*, *20*) inadequate. Instead, we defined complete switches by sequential crossing of two thresholds, set at two-thirds of the mean CW and CCW speeds (Fig. 2A, right panel). A typical switch event is displayed in detail in Fig. 2B. Filtering, which is required to show the CW and CCW speeds clearly, extends the apparent duration of a switch (Fig. 2B, left panel), but its finite duration is evident in the unfiltered data (Fig. 2B, center and right panels). Switches were observed with a broad range of durations across the population (Fig. 2, B to D) and within each cell record (see fig. S2 for an example set). Some switches require more than one revolution for completion, and not all switches vary in speed monotonically through the event. For example, the switch in Fig. 2D

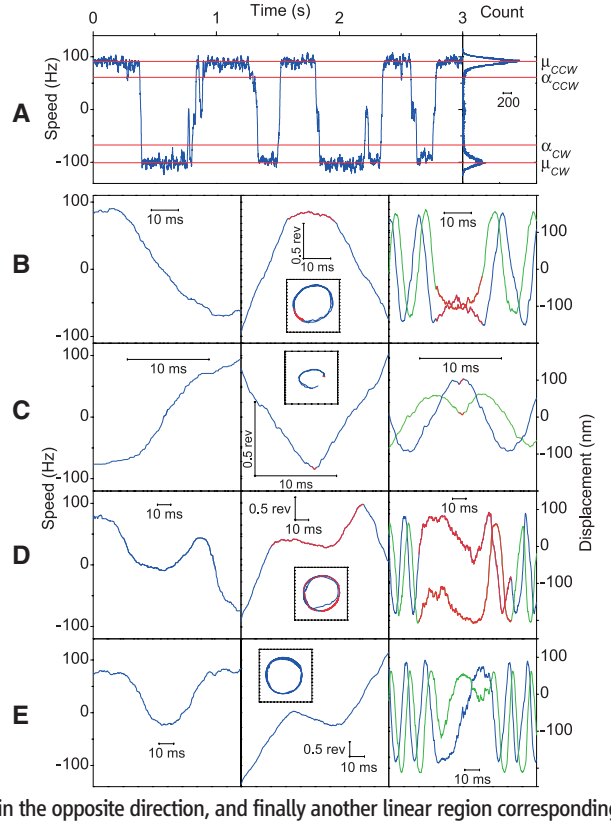

Fig. 2. Experimental evidence of conformational spread. (**A**) (Left) Three seconds of a typical motor speed record, median filtered (100 points) to reduce noise (for the full record, see fig. S1). Complete and incomplete switches are evident. (Right) The motor speed histogram for the full 30-s record. Because the peak shape is asymmetrically affected by incomplete switching, Gaussian curves were fitted to the outside portion of the histogram peaks to obtain mean speeds μ_{CCW} and μ_{CW} (*22*). Thresholds for the identification of complete switches were set at $\alpha_{CCW} = \alpha\ \mu_{CCW}$ and $\alpha_{CW} = \alpha\ \mu_{CW}$, with $\alpha = 2/3$. (**B**) (Left) Median filtered speed trace showing a typical complete switch. (Center) The same switch shown as unfiltered bead angle versus time. Scale bars show 0.5 revolutions and 10 ms. The switch comprises a linear region corresponding to smooth CCW rotation, followed by a central region corresponding to deceleration, reversal, and acceleration in the opposite direction, and finally another linear region corresponding to smooth CW rotation. The duration of the switch (20.8 ms, in red) was calculated as the interval during which the slope of the angle trace was statistically significantly different from that of the CW and CCW states in the whole 30-s motor trace (*22*). The inset shows the unfiltered bead trajectory (*x*, *y*) for the same switch. All insets show a range of 400 nm in *x* and *y* bead position. (Right) The same data as the inset in (B), center, shown as unfiltered bead position versus time (*x* in blue, *y* in green, switch in red). Sinusoidal sections of the trace correspond to smooth rotation; the sign of the phase shift between *x* and *y* indicates the direction of rotation. (**C** to **E**) Other typical switch events, plotted as in (B). (C) A fast switch of duration 1.4 ms. (D) A slow switch of duration 78.4 ms, taking almost one revolution to complete and demonstrating nonmonotonic speed variation. (E) An incomplete switch leading to transient reversal of rotation.

includes three reversals of direction before completion.

Incomplete switches were present in all records of switching cells but absent in a nonswitching *E. coli* strain (fig. S3), excluding the possibility that these events were artifacts of the rotation assay. A typical incomplete switch in the median filtered speed record is shown in detail in Fig. 2E. Incomplete switches to a variety of speed levels are observed, including levels that result in transient reversal of rotation. The histogram of speeds (Fig. 2A, right panel) for any given record does not clearly identify preferred speed levels, such as stops, during incomplete switch events. However, incomplete switches may explain "pauses" observed previously in measurements with lower angular and time resolution (*25*).

Independent evidence for multistate behavior was obtained using an optical trap (*26*) to stall pairs of 0.5-μm beads attached to switching motors. Bead pairs rotated through ~90° in a fixed optical trap when the direction of motor torque reversed. Complete switches of finite duration and incomplete switching were observed (fig. S4), as with the rotating beads.

We used Monte Carlo simulations (*22*) of the conformational spread model of the bacterial flagellar switch for comparison to our experimental results. The kinetic parameters (Fig. 3, legend) were fixed to the values $\omega_b = 10\ s^{-1}$ and $\omega_a = 10^4\ s^{-1}$, following previous studies (*4*, *12*), whereas the thermodynamic parameters E_A and E_J (Fig. 1) were chosen to match the mean experimental values at CW bias 0.5 of complete switch durations and of intervals between complete switches (*22*). The simulated CheY-P concentration was varied to obtain the desired bias in each simulation. To allow direct comparison between the conformational spread model and experimental data, we assumed a linear dependence of motor speed on the number of active protomers in the ring. This assumption is based on the motor containing a large number of independent units (*27*), each of which generates constant torque in a direction specified by the state of the nearest rotor protomer (Fig. 1). A Langevin simulation modeled the viscous load of the bead connected to the motor by a flexible tether, thereby converting simulated activity on the ring (Fig. 3A) into rotation angle of the bead (Fig. 3B) (*22*). Simulated records (Fig. 3) are qualitatively indistinguishable from experimental records (Fig. 2) and were analyzed using identical methods. Figure 3 shows fast (C) and slow (D) complete switches and incomplete switches (E) for comparison to Fig. 2, C to E.

We made a detailed quantitative comparison between the experimental data and the predictions of the conformational spread model. To exclude possible artifacts due to the rotation assay, we analyzed only cell records, switches, and intervals between switches that satisfied strict sets of criteria (*22*). Figure 4A shows switch duration distributions for experimental (blue) and simulated (red) data. The distributions are indistinguishable, each with a peak at ~8 ms and a standard deviation of ~15 ms, in addition to the fitted mean of ~20 ms. The shortest switches last less than 2 ms, whereas the longest last more than 100 ms. Switch durations are not correlated with position of the event in the orbit (*22*), and distributions for subsets of the data sorted according to motor bias and switch direction showed no clear dependence on either (Fig. 4A, inset). The distribution of durations cannot be explained as an artifact of elasticity in the hook-bead system: Using the largest published experimental estimate of hook compliance (*28*), the simulated hook-bead response time for a 0.5-μm diameter bead is approximately 0.7 ms (*22*). Additionally, we performed experiments and simulations using 0.35-μm diameter beads. The underlying switch duration distribution, obtained by deconvolution of the experimental distribution and the simulated hook-bead response time distribution, was independent of bead size (*22*).

We also compared the distribution of intervals between complete switches. Complete switches were detected using the dual-threshold scheme of Fig. 2A (*22*), allowing intervals to be defined without sensitivity to incomplete switches that might otherwise skew the distributions toward a shorter time scale. Figure 4B (top) shows interval distributions at three different values of bias, to compare switching kinetics at different CheY-P concentrations (*20*) (see fig. S6 for other biases). Both experimental (blue) and simulated (red) intervals are exponentially distributed in the measured range (up to ~10 s) with bias-dependent mean interval lengths (Fig. 4B, bottom). Mean interval lengths are robust to at least ±20% variations in threshold and median filter level (fig. S7). Analysis of the protomer states underlying the simulation does not change the distributions, indicating that missed events are not important in our analyses (*22*) and that incomplete switches are not artifacts of unresolved fast pairs of complete switches. Our results are in contrast to a recent study that measured gamma-distributed intervals (*20*). It is possible that gamma distributions were an artifact of attaching beads to long filaments (*29*). Alternatively, switching kinetics may have been different because of the permanently active CheY mutant used.

We quantified incomplete switching as a further independent test of agreement between data and the conformational spread model. An incomplete switch in a CCW interval was defined by a downward crossing of the threshold β_{CCW} =

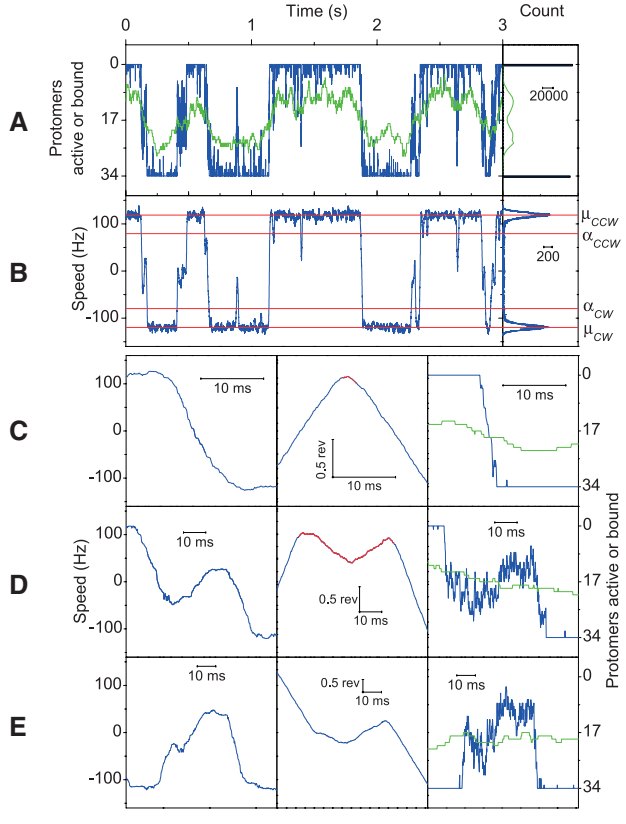

Fig. 3. Simulation of the conformational spread model. We calculated rate constants for CheY-P binding using $k_{b\to B} = (c/c_{0.5})\omega_b$, $k_{B\to b} = \omega_b \exp(-\Delta G^*_{B\to b}/k_BT)$, where ω_b is the characteristic binding rate, $c/c_{0.5}$ is the concentration of CheY-P relative to that required for bias = 0.5, and $\Delta G^*_{B\to b} = \pm E_A$ is the free-energy difference of unbinding at $c = c_{0.5}$ (Fig. 1). We calculated rate constants for conformational change of the protomers using $k_{ij} = \omega_a \exp(-\Delta G_{ij}/2k_BT)$, where ω_a is the characteristic rate of conformational changes, and the free-energy difference of a transition from state *i* to state *j*, ΔG_{ij}, includes the effects of binding energy (Fig. 1B) and interactions (Fig. 1C). A more general description of the parameters of the conformational spread model is given in (*22*). (**A**) (Left) Three seconds of a typical unfiltered simulation record of the conformational spread model, showing the number of active protomers in the ring (blue) and the number of CheY-P molecules bound (green). (Right) Activity and binding histograms for the full 30 s record. (**B**) (Left) The corresponding simulated speed record for direct comparison to experimental data, median filtered (100 points), and including the effect of the bead linkage as described (for the full record, see fig. S5). (Right) The simulated speed histogram for the full 30-s record. (**C** to **E**). Typical fast (1.7 ms) (C), slow (32.5 ms) (D), and incomplete (E) simulated switch events, displayed as in Fig. 2, B to E, except that the right-hand column shows the number of active protomers (blue) and bound CheY-P molecules (green) in the simulation. Simulated records show the same behavior as experimental data.

$\beta \times \mu_{CCW}$ in the median-filtered speed record (*22*), followed by an upward crossing of the threshold α_{CCW}. Incomplete switches in CW episodes were defined similarly. The intervals between incomplete switches were exponentially distributed in both experimental and simulated data for $\beta = 1/3$ (Fig. 4C, top). The mean interval between incomplete switches from the CCW (CW) state increased with CCW (CW) bias (Fig. 4C, bottom), with broad agreement between experimental and simulated data. The number of incomplete switches detected clearly depends on the parameter β. The mean interval length for the largest data bin (CW bias 0.2) decreased linearly with β in both experiment and simulation, becoming identical to the mean interval length between complete switches as $\beta \rightarrow -2/3$ (Fig. 4C, bottom, inset). For these values of β, intervals remained exponentially distributed (fig. S9). No attempt was made to adjust the model parameters to fit the experimental data on incomplete switches: The agreement may improve upon an exhaustive search of the model's parameter space.

Bacterial flagellar switching has classically been understood in terms of the two-state concerted allosteric model (*16*). A recent study used the conformational spread model to explain the dependence of switching rates on load (*30*). We have observed multistate switching, which is the signature of conformational spread. Switch events are not instantaneous but show a broadly distributed duration, and incomplete switching is prevalent. Exponentially distributed intervals between complete switches demonstrate that switching approximates a two-state Poisson process at lower time resolution, despite the underlying multistate nature of the switch, in agreement with early two-state phenomenological models (*18*, *19*). Conformational spread is able to reproduce these observations with remarkable quantitative agreement, despite the very limited search of the model parameter space and using only data collected at neutral bias to guide this search. As a final comparison, we constructed a Hill plot (Fig. 4D) to confirm the sensitivity of the simulated switch. The model accurately reproduces previously measured values of the binding (*12*, *13*) and switching (*10*) cooperativity, with Hill coefficients 3.5 and 9.4, respectively. Taken together, this is compelling evidence that the conformational spread model accurately represents the flagellar switch.

Recent advances in resolving the functional states of a number of other proteins have necessitated extensions of the classical models of allostery, even to describe relatively small protein complexes (*31*, *32*). Modern theoretical treatments of allosteric regulation indicate that the conformational heterogeneity that results from stochastic coupling, both between different subunits and between binding and conformation, may be a selectable trait (*33*). With the classical models encompassed at the parameter space limits of the conformational spread model, which can be extended to geometries other than a ring (*4*, *8*), we expect the model to be generally useful in understanding protein cooperativity and signal regulation.

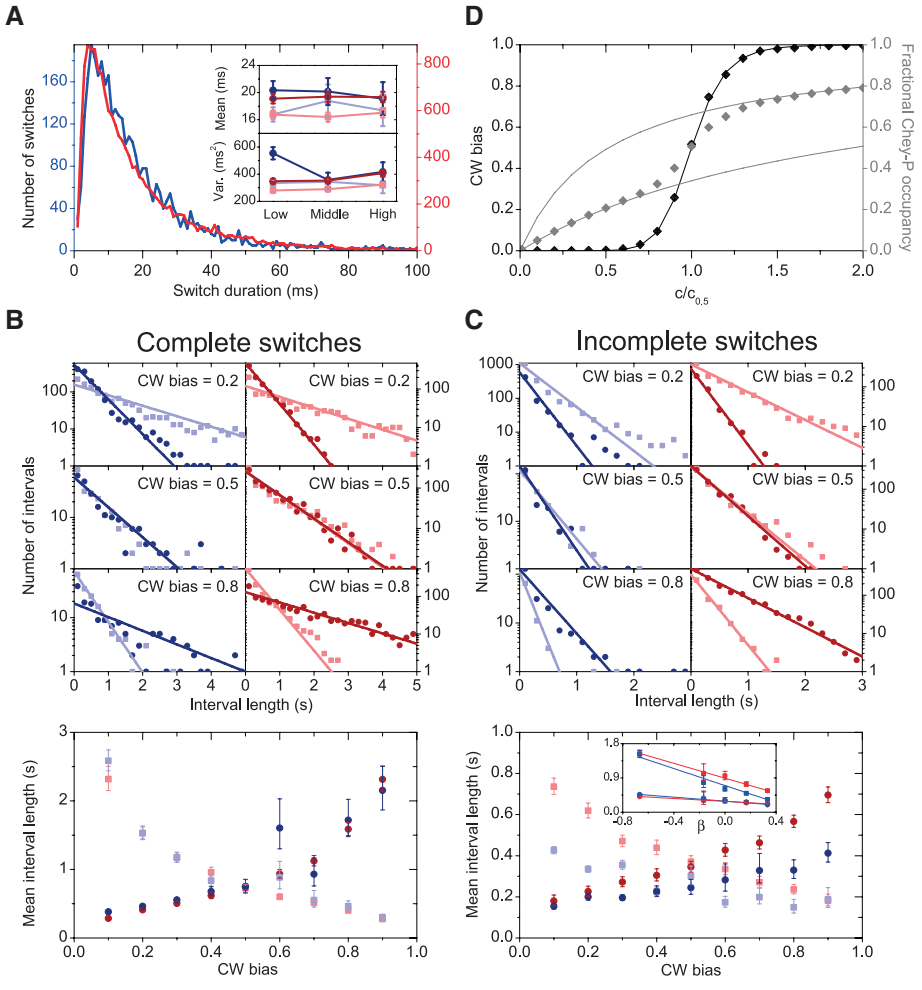

Fig. 4. Quantitative analysis of experimental and simulated switching. Experimental data are in blue, simulation data are in red. CW data are represented by dark circles, CCW data by light squares. Error bars are 99% confidence intervals unless stated otherwise. (**A**) Switch duration distributions for all complete switches analyzed. (Inset) Mean and variance of switch durations for CW-to-CCW (light-colored data points) and CCW-to-CW (dark-colored data points) switches for different ranges of CW bias (low = 0 to 1/3, 2459 switches; middle = 1/3 to 2/3, 521 switches; high = 2/3 to 1, 599 switches). (**B**) (Top) Distributions of intervals between complete switches at a range of CW bias values (0.2 ± 0.05, 0.5 ± 0.05, 0.8 ± 0.05, top to bottom). Lines are exponential maximum likelihood fits applied to full data sets. (Bottom) Mean interval lengths obtained from the fits in (B), top. (**C**) Equivalent analysis as presented in (B), but for distributions of intervals between incomplete switches with $\beta = 1/3$. Data sets across the full bias range are shown in fig. S8. (Inset) Linear variation of mean interval lengths with β, using the CW bias bin with the largest amount of data (0.2 ± 0.05). Also plotted are the mean complete switch interval lengths from (B), equivalent to an analysis with $\beta = -2/3$. (**D**) Simulated bias (black diamonds) and fraction of protomers with CheY-P bound (gray diamonds) versus CheY-P concentration parameter ($c/c_{0.5}$). A Hill fit (not shown) to the simulated bias gave a Hill coefficient of 9.4, but the bias is also well fit (black line) using a Hill coefficient of 10.1 as experimentally determined previously (*10*). The simulated binding curve is bounded by the single-site Michaelis Menten dissociation curves for inactive (lower gray curve) and active protomers (upper gray curve), as expected from the model. Error bars showing standard errors of the mean are smaller than the symbols.

References and Notes

1. J. Monod, J. Wyman, J. P. Changeux, *J. Mol. Biol.* **12**, 88 (1965).
2. D. E. Koshland Jr., G. Némethy, D. Filmer, *Biochemistry* **5**, 365 (1966).
3. M. Eigen, *Nobel Symp.* **5**, 333 (1967).
4. T. A. J. Duke, N. Le Novère, D. Bray, *J. Mol. Biol.* **308**, 541 (2001).
5. T. A. J. Duke, D. Bray, *Proc. Natl. Acad. Sci. U.S.A.* **96**, 10104 (1999).
6. J. P. Changeux, S. J. Edelstein, *Science* **308**, 1424 (2005).
7. D. E. Koshland Jr., K. Hamadani, *J. Biol. Chem.* **277**, 46841 (2002).
8. D. Bray, T. Duke, *Annu. Rev. Biophys. Biomol. Struct.* **33**, 53 (2004).
9. Y. Sowa, R. M. Berry, *Q. Rev. Biophys.* **41**, 103 (2008).
10. P. Cluzel, M. Surette, S. Leibler, *Science* **287**, 1652 (2000).
11. D. Bray, *Proc. Natl. Acad. Sci. U.S.A.* **99**, 7 (2002).

12. V. Sourjik, H. C. Berg, *Proc. Natl. Acad. Sci. U.S.A.* **99**, 12669 (2002).
13. Y. Sagi, S. Khan, M. Eisenbach, *J. Biol. Chem.* **278**, 25867 (2003).
14. L. Stryer, *Biochemistry* (Freeman, New York, ed. 4, 1999).
15. L. Turner, S. R. Caplan, H. C. Berg, *Biophys. J.* **71**, 2227 (1996).
16. U. Alon *et al.*, *EMBO J.* **17**, 4238 (1998).
17. S. Kudo, Y. Magariyama, S. Aizawa, *Nature* **346**, 677 (1990).
18. S. M. Block, J. E. Segall, H. C. Berg, *J. Bacteriol.* **154**, 312 (1983).
19. B. E. Scharf, K. A. Fahrner, L. Turner, H. C. Berg, *Proc. Natl. Acad. Sci. U.S.A.* **95**, 201 (1998).
20. E. A. Korobkova, T. Emonet, H. Park, P. Cluzel, *Phys. Rev. Lett.* **96**, 058105 (2006).
21. Y. Sowa *et al.*, *Nature* **437**, 916 (2005).
22. Materials and methods are available as supporting material on *Science* Online.
23. W. S. Ryu, R. M. Berry, H. C. Berg, *Nature* **403**, 444 (2000).
24. E. Korobkova, T. Emonet, J. M. G. Vilar, T. S. Shimizu, P. Cluzel, *Nature* **428**, 574 (2004).
25. I. R. Lapidus, M. Welch, M. Eisenbach, *J. Bacteriol.* **170**, 3627 (1988).
26. T. Pilizota *et al.*, *Biophys. J.* **93**, 264 (2007).
27. S. W. Reid *et al.*, *Proc. Natl. Acad. Sci. U.S.A.* **103**, 8066 (2006).
28. S. M. Block, D. F. Blair, H. C. Berg, *Nature* **338**, 514 (1989).
29. S. B. van Albada, S. Tănase-Nicola, P. R. ten Wolde, *Mol. Syst. Biol.* **5**, 316 (2009).
30. J. Yuan, K. A. Fahrner, H. C. Berg, *J. Mol. Biol.* **390**, 394 (2009).
31. C. Viappiani *et al.*, *Proc. Natl. Acad. Sci. U.S.A.* **101**, 14414 (2004).
32. J. W. Karpen, M. Ruiz, *Trends Biochem. Sci.* **27**, 402 (2002).
33. V. J. Hilser, E. B. Thompson, *Proc. Natl. Acad. Sci. U.S.A.* **104**, 8311 (2007).
34. C. M. Dyer, A. S. Vartanian, H. Zhou, F. W. Dahlquist, *J. Mol. Biol.* **388**, 71 (2009).
35. S. M. Van Way, S. G. Millas, A. H. Lee, M. D. Manson, *J. Bacteriol.* **186**, 3173 (2004).
36. S. Y. Park, B. Lowder, A. M. Bilwes, D. F. Blair, B. R. Crane, *Proc. Natl. Acad. Sci. U.S.A.* **103**, 11886 (2006).
37. Special thanks to T. Duke and I. Graham for introducing the conformational spread model to us. We also thank H. C. Berg and K. Fahrner for the gift of strain KAF 84 and KAF 95. The research of F.B., T.P. and R.M.B. was supported by the European Research Grant NANOMOT (Synthetic Biomimetic Nanoengines: A Modular Platform for Engineering of Nanomechanical Actuator Building Blocks), that of B.C.S. by a fellowship from the European Molecular Biology Organisation, that of D.V.N. by the Devorguilla Scholarship from Balliol College and the Clarendon Scholarship from Oxford University, that of P.K.M. partially by a Royal Society Wolfson Research Merit Award, and that of R.W.B. by the Engineering and Physical Sciences Research Council. F.B. also thanks Y. Zhang for help with the analysis program.

Supporting Online Material
www.sciencemag.org/cgi/content/full/327/5966/685/DC1
Materials and Methods
Figs. S1 to S13
References
Movie S1

17 September 2009; accepted 17 December 2009
10.1126/science.1182105

Cryo-EM Model of the Bullet-Shaped Vesicular Stomatitis Virus

Peng Ge,[1,2,3,4] Jun Tsao,[5] Stan Schein,[2,6] Todd J. Green,[5] Ming Luo,[5] Z. Hong Zhou[1,2,3,4]*

Vesicular stomatitis virus (VSV) is a bullet-shaped rhabdovirus and a model system of negative-strand RNA viruses. Through direct visualization by means of cryo–electron microscopy, we show that each virion contains two nested, left-handed helices: an outer helix of matrix protein M and an inner helix of nucleoprotein N and RNA. M has a hub domain with four contact sites that link to neighboring M and N subunits, providing rigidity by clamping adjacent turns of the nucleocapsid. Side-by-side interactions between neighboring N subunits are critical for the nucleocapsid to form a bullet shape, and structure-based mutagenesis results support this description. Together, our data suggest a mechanism of VSV assembly in which the nucleocapsid spirals from the tip to become the helical trunk, both subsequently framed and rigidified by the M layer.

Vesicular stomatitis virus (VSV) is an enveloped, bullet-shaped, non-segmented, negative-strand RNA virus (NSRV) belonging to the rhabdovirus family, which includes the rabies virus. Because some attenuated VSV strains are nontoxic to normal tissue, VSV has therapeutic potential as an anticancer agent and vaccine vector (*1*, *2*). Furthermore, pseudotypes of VSV carrying receptors for HIV proteins can selectively target and kill HIV-1–infected cells and control HIV-1 infection (*3*, *4*).

[1]Department of Microbiology, Immunology, and Molecular Genetics, University of California at Los Angeles (UCLA), Los Angeles, CA 90095-7364, USA. [2]California NanoSystems Institute, UCLA, 237 BSRB, 615 Charles E. Young Drive South, Los Angeles, CA 90095-7364, USA. [3]Structural Computational Biology and Molecular Biophysics Program, Baylor College of Medicine, Houston, TX 77030, USA. [4]Department of Pathology and Laboratory Medicine, University of Texas Medical School at Houston, Houston, TX 77030, USA. [5]Department of Microbiology, University of Alabama at Birmingham, Birmingham, AL 35294, USA. [6]Department of Psychology, UCLA, Los Angeles, CA 90095-7364, USA.

*To whom correspondence should be addressed. E-mail: hong.zhou@ucla.edu

Whereas many other NSRVs are pleomorphic, VSV has a rigid "bullet" shape. Attempts to visualize its organization by means of negatively stained electron microscopy (EM) have resulted in limited two-dimensional (2D) pictures: The virion has a lipid envelope (decorated with G spikes) that encloses a nucleocapsid composed of RNA plus nucleoprotein N and an associated matrix formed by M proteins. In recent years, crystal structures of components of VSV have been determined: the C-terminal core domain M_{CTD} of the matrix protein (M) (*5*, *6*), the nucleoprotein (N) (*7*), the partial structure of phosphoprotein (P) (*8*), the complex of N with the C-terminal of P (*9*), and the two forms of the ectodomain of the glycoprotein (G) (*10*, *11*). The large polymerase (L) still awaits structure determination. However, how these proteins assemble into the characteristic rigid bullet-shaped virion has not been clear. Here, we report the 3D structure of the helical portion (the "trunk") of the VSV virion as determined by means of cryo-electron microscopy (cryo-EM) as well as a study of the bullet-shaped tip from an integrated image-processing approach. This analysis leads us to propose a model for assembly of the virus with its origin at the bullet tip.

Cryo-EM images of purified VSV virions show intact bullet-shaped particles almost devoid of truncated or defective interference particles (Fig. 1A). The reconstructed map of the virion trunk (Fig. 1B and movies S1 and S2) has an effective resolution of 10.6 Å based on the 0.5 Fourier shell correlation coefficient criterion (fig. S2). We were able to dock crystal structures of the C-terminal domain of M [Protein Data Bank (PDB)1LG7 or 2W2R] (*5*, *6*) and all of N (PDB 2GIC) (*7*) into our cryo-EM density map. The matching of several high-density regions in the cryo-EM map with α helices in the docked atomic models (Fig. 2A, M, and Fig. 3A, N) supports the validity of the cryo-EM map. These dockings also establish the chirality of the structure.

When reconstructed with a helical symmetry imposed (*12*), the 3D map includes an outermost lipid bilayer, a middle layer composed of a helix-based mesh of M, and an innermost condensed nucleocapsid composed of a helically organized string of N subunits and RNA (Fig. 1, B and C, and fig. S3). [The M (Fig. 2A) and N (Fig. 3A) layers were identified on the basis of their close match with their crystal structures of M (*5*, *6*) and N (*7*).] Each of the N and M layers consists of a single helix (1-start helix). Although the interior of the nucleocapsid contains a denser region than background, no density was found that was reasonably attributable to individual P or L subunits, suggesting that those are organized in a lower-symmetric or asymmetric fashion [supporting online material (SOM) text]. A layer of density outside the membrane may be identified as G protein (fig. S1) because the G protein is the only envelope protein in VSV. However, individual G spikes cannot be resolved in this layer, possibly because of flexibly attached ectodomains or inconsistent symmetry, and this layer of density